Water Resources Research

RESEARCH ARTICLE
10.1029/2025WR042627

Increased Dependency on Extreme Precipitation in a Warmer Climate

Mohammed Ombadi[1,2], Lisa Nguyen[1], Srishti Gaur[1], Andrew Gronewold[3], and Peter B. Reich[2,3]

[1]Department of Climate & Space Sciences & Engineering, University of Michigan, Ann Arbor, MI, USA, [2]Institute for Global Change Biology, University of Michigan, Ann Arbor, MI, USA, [3]School for Environment and Sustainability, University of Michigan, Ann Arbor, MI, USA

Key Points:

- Extreme Precipitation Dependency Index increases substantially beyond the UN's mitigation targets, with some regional increases exceeding 20%
- Global rain-fed croplands, particularly those in low-income countries, are likely to be adversely impacted by extreme precipitation
- Urgent need to limit global warming to 1.5–2 degree Celsius to mitigate widespread socio-environmental consequences

Supporting Information:

Supporting Information may be found in the online version of this article.

Correspondence to:

M. Ombadi,
ombadi@umich.edu

Citation:

Ombadi, M., Nguyen, L., Gaur, S., Gronewold, A., & Reich, P. B. (2026). Increased dependency on extreme precipitation in a warmer climate. *Water Resources Research*, *62*, e2025WR042627. https://doi.org/10.1029/2025WR042627

Received 16 OCT 2025
Accepted 11 MAR 2026

© 2026. The Author(s).
This is an open access article under the terms of the Creative Commons Attribution License, which permits use, distribution and reproduction in any medium, provided the original work is properly cited.

Abstract Growing evidence suggests that extreme precipitation increases over most regions globally as the climate warms. However, it remains poorly understood how the fraction of annual precipitation from extreme events changes due to warming-induced alteration of both annual and extreme precipitation patterns. Understanding such changes is crucial for water resources and agricultural planning and management. Here, we propose the Extreme Precipitation Dependency Index (EPDI), a robust metric to quantify the relative contribution of extreme precipitation to annual totals under a warming climate. Using both climate model projections and observational data sets, we find that EPDI increases considerably beyond the UN's mitigation targets, with many global land regions experiencing a 15%–20% rise at 4°C warming. Hotspots include the African Sahel, Southeast Asia, Northern Australia, and the Amazon. Observations reveal that many regions are already experiencing increases in extreme precipitation contributions at rates exceeding model projections. We further explore the implications of these trends on rain-fed agriculture, reservoir operations, and ecosystem health. Our analysis indicates that 54%–96% of global rain-fed croplands may be adversely affected, alongside significant risks to boreal forests. These results reveal that low-income countries, particularly those dependent on rain-fed agriculture, are projected to receive a larger fraction of their annual precipitation from extreme events, likely resulting in reduced productivity and economic disruption. Overall, this underscores the urgent need to limit global warming to 1.5–2°C to mitigate widespread socio-environmental consequences.

Plain Language Summary The intensity of extreme rainfall events increases as our planet gets warmer. But so far, it's not clear how the fraction of annual rainfall that comes from extreme events changes as a result of global warming. To better understand this, we propose a new metric, the Extreme Precipitation Dependency Index (EPDI), which estimates how much annual rainfall comes from extreme events, particularly in warmer climates. Climate model projections utilized in this study show a considerable increase in EPDI beyond the UN's climate targets. At 4 degree Celsius of warming, many global land areas could see a 15%–20% increase in rainfall from extreme events. The most affected regions across the world include the African Sahel, Southeast Asia, Northern Australia, and the Amazon. We also examined the potential impact of an increase in the EPDI on rainfed agriculture, which shows that more than half of the global croplands will potentially be adversely affected by this increase. These changes are likely to hit low-income countries the hardest, as they rely heavily on rain-fed agriculture—putting their food security and economies at risk. It is crucial to limit global warming to a lower level (1.5–2 degree Celsius) to reduce these risks.

1. Introduction

Over the past few decades, there has been growing evidence that the intensity of daily and sub-daily extreme precipitation increases at the global scale at a rate of approximately 7% per 1°C of warming, which is consistent with rates expected by the Clausius-Clapeyron (C-C) relationship (Allen & Ingram, 2002; Pall et al., 2006; Seneviratne et al., 2021; Wasko et al., 2021). However, at regional scales, increases in extreme precipitation are further modulated by several factors including but not limited to changes in upward velocities and atmospheric circulations (Chen et al., 2019; O'Gorman & Schneider, 2009; Pfahl et al., 2017), snow fraction of precipitation (Ombadi et al., 2023), urbanization (Zhang et al., 2018) and irrigation (Alter et al., 2015). These regional factors can lead to increases in the intensity of precipitation extremes at rates higher than that predicted by C-C, which have been both observed and projected at daily (Bao et al., 2017; Ombadi et al., 2023) and sub-daily time scales (Ayat et al., 2022; Ombadi et al., 2023; Westra et al., 2014). On the other hand, changes in mean annual

precipitation, hereafter referred to as annual precipitation, are spatially heterogeneous. For instance, earlier studies found that annual precipitation increases over dry global land regions, while showing no statistically significant change in wet regions (Donat et al., 2016). More recent studies reveal substantial spatial variability in observed changes of annual precipitation, with both increasing and decreasing trends (Dai, 2021; Douville et al., 2021). Even in regions where annual precipitation increases, the rate of increase is lower than that of extreme precipitation.

The differences in the rate of change between annual and extreme precipitation can be attributed primarily to energy budget constraints. That is, the change in annual precipitation is not controlled by the availability of moisture in the lower troposphere (i.e., C-C relationship), but rather by the radiative cooling ability of the troposphere to balance the latent heat released by precipitation (Allen & Ingram, 2002; Pendergrass & Hartmann, 2014). As a result, annual precipitation at the global scale increases at a rate considerably lower than that of C-C, with earlier estimates of 3.4% per 1°C of warming (Allen & Ingram, 2002) and more recent estimates of 2.1%–3.1% per 1°C (Pendergrass, 2020). Conversely, precipitation extremes at daily and sub-daily time scales typically occur when the total available moisture in the atmosphere is precipitated (Allen & Ingram, 2002; Trenberth, 1999; Trenberth et al., 2003), with negligible energy budget constraints.

As a corollary to these differences in the behavior of mean and extreme precipitation in response to warming, it has been hypothesized that the amount of precipitation falling within extreme events will be at the expense of that falling within moderate and light precipitation events (Trenberth, 1999; Trenberth et al., 2003), thereby increasing the unevenness of precipitation distribution, with more precipitation falling within a fewer days of the year. This hypothesis is challenged by previous studies showing that the unevenness of daily precipitation distribution is not increasing across all regions globally (Rajah al., 2014). However, at regional scales, analysis of a century-long observational data set across the contiguous United States showed that the increase in extreme daily precipitation is contributing disproportionally to annual precipitation, with over half of the increase in annual precipitation due to trends in daily events above the 90th percentile (Karl & Knight, 1998). Evidence of increasing precipitation from extreme events (above certain thresholds; e.g., 95th or 99th) have also been observed at local scales such as the Southern Mid-Atlantic United States (Dollan et al., 2022). Recent work has also provided valuable insights on the unevenness of daily precipitation across global land regions, showing that on average half of annual precipitation falls within only 12 days in the year, with such unevenness projected to increase in a warmer climate (Pendergrass & Knutti, 2018). However, despite this focus on understanding the distribution of daily precipitation and its changes due to global warming, direct and quantitative estimation of changes in the fraction of annual precipitation from extreme events at different global warming levels (GWLs) remains elusive. Such quantification is important in order to inform mitigation and adaptation efforts in accord with the United Nations Paris Agreement goals. Furthermore, it remains unclear whether certain regions are at more risk of increases in the fraction of annual precipitation from extremes, whether such projections are consistent with observed changes over the past decades, and how would such changes affect both human systems and ecosystems.

Here, we propose a new index to understand and quantify the contribution of extreme events to annual precipitation. Our index, the EPDI, is defined as the amount of precipitation in very wet days above the 95th percentile (R95p) relative to mean annual precipitation (see Materials and Methods). We utilize both climate model projections from the sixth phase of the Coupled Model Intercomparison Project (CMIP6, Table 1) (Eyring et al., 2016) and observational data sets (Dunn et al., 2020) to examine changes in the EPDI. Our results show that the EPDI exhibits a substantial increase at warming levels beyond the UN mitigation targets, with some regional increases exceeding 20%. At such warming levels, clear patterns of regional hotspots emerge, including large parts of South America and Africa. Moreover, we show that the projected spatial patterns of regional hotspots are largely consistent with those obtained from observational data sets over the past seven decades. Finally, we conclude by demonstrating three important impacts of these changes on rain-fed agriculture, water resources management, and forest health, while illustrating how changes in the EPDI relate to changes in the entire distribution of daily precipitation.

Table 1
List of the Seven CMIP6 Models Used in This Study With Their Name, Institution and Spatial Resolution

Model	Institute	Resolution [°]
CESM2-WACCM	NCAR National Center for Atmospheric Research, United States	1 × 1
CMCC-CM2-SR5	Fondazione Centro Euro-Mediterraneo sui Cambiamenti Climatici, Italy	1 × 1
EC-Earth3	EC-Earth Consortium, Europe	1 × 1
GFDL-ESM4	National Oceanic and Atmospheric Administration, Geophysical Fluid Dynamics Laboratory, United States	1 × 1
INM-CM4-8	Institute for Numerical Mathematics Russian Federation, Russia	1.5 × 1.5
MPI-ESM1-2-HR	Max Planck Institute for Meteorology, Germany	1 × 1
TaiESM1	Research Center for Environmental Changes, Taiwan	1 × 1

Note. Each model realization was taken from the first ensemble run or the "r1i1p1f1" run.

2. Materials and Methods

2.1. Selection of Data Sets

Climate model simulations: for the analysis of projected changes in EPDI, we utilized 7 Earth System Models (ESMs) that participated in the 6th phase of the CMIP6 (Eyring et al., 2016). The 7 models were chosen to get a spread in the physics, climate sensitivity, and dynamical properties of the ESMs taking part in CMIP6. Table 1 shows the list of the 7 models, their institutions, and spatial resolutions. For each model, we used the historical CMIP6 scenarios for the period 1950–1979 to estimate EPDI in baseline climate, while projected changes were obtained from the Shared Socioeconomic Pathway (SSP) scenarios for the period 2015–2100, which represent different mitigation and emissions forcings. We used the ssp126, ssp245, ssp370, and ssp585 projected scenarios, which range from low emissions to high emissions, respectively. This resulted in 28 unique projected data sets (7 ESMs * 4 SSPs); for each model and SSP scenario, we used the first ensemble realization, corresponding to the "r1i1p1f1" identifier. For all data sets, the variable precipitation "pr" was downloaded at daily time scale for the entire global domain.

Observed precipitation: In order to compare the historical estimates of EPDI from CMIP6 models to those estimated from observations, we used the Gridded Land Surface Extremes Indices (HadEX3) (Dunn et al., 2020). This data set provides wide coverage with assimilated station data from 17,000 precipitation stations provided on a 1.25° latitude by 1.875° longitude grid for the period 1901 to 2018. To ensure consistency with the CMIP6 data, we have used the period 1950–1979 as the baseline of our analysis for the HadEX3 data set. Additionally, we used the period 1980–2009 as the recent past period to examine observed changes in EPDI. At the global scale, HadEX3 data set provides adequate coverage to evaluate the estimates from CMIP6 models. Here, two variables were utilized from the HadEX3 data set: (a) annual total precipitation (PRCPTOT), which is the annual precipitation totals from days that receive ≥1 mm of rain; (b) annual precipitation from very wet days (R95p), which is the annual total precipitation from days that receive > the 95th percentile of wet days. This is essentially the amount of rain accumulated in the top 5% of wet days (commonly referred to as very wet days). Here, we have used HadEX3 due to its comprehensive analysis of in situ observations and suitability for analysis of extreme meteorological variables as recommended by World Meteorological Organization Expert Team on Climate Change Detection and Indices (ETCCDI, Dunn et al., 2020). HadEX3 and its pervious version have been commonly used in studies on extreme precipitation (e.g., Asadieh & Krakauer, 2015; Dunn et al., 2022).

Rain-fed and irrigated cropland data for assessment of the global rain-fed agricultural land exposed to changes in EPDI: we used the Landsat-Derived Global Rainfed and Irrigated-Cropland Product 30 m V001 (LGRIP30) satellite data (Teluguntla et al., 2023). LGRIP30 identifies both rain-fed and irrigated croplands over the period 2014–2017, giving an integrated snapshot of the worlds croplands in an average 2015 product. Irrigated croplands are defined if at least one artificial irrigation system is used. The data is gridded to a nominal resolution of 30 by

30 m and covers the whole globe. Only data from 60° South to 70° North was downloaded because the high latitudes had no croplands.

2.2. Re-Gridding to a Common Spatial Resolution

In order to assess changes in the multi-model mean, all CMIP6 model data was resampled to a common spatial resolution of (1° × 1°) using bilinear interpolation. In order to eliminate any potential bias due to resampling, we carried out all calculations first before resampling. It should be noted that multi-model mean data was calculated using simple averaging with equal weights applied to all models. The LGRIP30 data was re-gridded bilinearly to a 1° × 1° resolution to match that of the CMIP6 models before it was used for the analysis carried out in the present study.

2.3. Computation of Regional Averages

To aggregate results at regional (sub-continental) scales, we used the scientific land regions used in the Sixth Assessment Report of the Intergovernmental Panel on Climate Change (IPCC-AR6; Calvin et al., 2023; Iturbide et al., 2020). These regions are grouped together because they have similar regional climate features that are distinct from their neighbors. There are 61 regions consisting of 46 land and 15 ocean regions (the exact boundaries of these 46 land regions are shown in Figure S1 in Supporting Information S1). In the present study, we only focused on the land regions, excluding the 2 Antarctic regions. Note that these are land regions, but can also contain ocean and lake areas, for instance the Mediterranean. To define the regions and carry out the associated analysis, we used the MIT licensed python package regionmask (Hauser et al., 2016). In addition to the land regions defined in IPCC AR6, we define the African Sahel as a separate region (Figure S1 in Supporting Information S1). This choice is motivated by our results, which reveal distinct signals of EPDI change across this region, spanning parts of the Sahara Desert, Western Africa, Central Africa, and northeastern Africa.

2.4. Identifying Global Warming Levels for Earth System Models

The CMIP6 models vary in their climate sensitivities (the change in mean global temperature in response to radiative forcing). For instance, under the same SSP scenario, some models project global warming increases of 3°C by the end of the century while others project 5°C. In order to remove model biases, we look at changes of variables relative to GWL instead of emission scenarios. To define a warming level, we used the Transient GWLs for CMIP6 data (Hauser et al., 2022), which reports the 20 years time period where the average global temperature anomaly relative to 1850–1900 reached +1.5°C, +2°C, +3°C, or +4°C. For each model and SSP that reached +1.5,+2,+3, or +4°C, we used the corresponding 20 years time period for our analysis. Based on the 7 ESMs used in this study, there were 15, 18, 13, and 6 model realizations for the 1.5, 2, 3, and 4°C warming levels, respectively. Details of the ensembles used at each warming level, with a list of models and SSP scenarios is shown in Table S1 in Supporting Information S1.

2.5. Calculating the Extreme Precipitation Dependency Index (EPDI)

For a given year (t) in any grid cell (i), the long-term EPDI is defined as follows:

$$\mathrm{EPDI} = \frac{1}{n}\sum_{t=1}^{n}\frac{R95p_{(i,t)}}{P_{(i,t)}} \tag{1}$$

Where $R95p_{(i,t)}$ is the amount of precipitation in grid cell i and year t from very wet days (above the 95th percentile) as defined by the ETCCDI, while $P_{(i,t)}$ is the annual precipitation of year t in grid cell i. R95p is calculated by summing precipitation amounts in days above the 95th percentile. In order to account for regional differences in the length of the precipitation season, we only consider wet days (daily precipitation ≥1 mm; including both rainfall and snowfall). This means that in regions with a precipitation season length of 20 days or less, R95p is equivalent to the annual maximum daily precipitation (Rx1day). On the other hand, annual precipitation P is calculated by summing all daily precipitation amounts in a year, including those with less than 1 mm of precipitation.

For any grid cell, the projected and observed changes in the fraction of extremes to total precipitation, ΔEPDI, is calculated as follows:

$$\Delta\text{EPDI} = \left(\frac{\text{EPDI}_{\text{future}} - \text{EPDI}_{\text{hist}}}{\text{EPDI}_{\text{hist}}}\right) \times 100\% \quad (2)$$

Where $\text{EPDI}_{\text{hist}}$ is the estimate of EPDI in all i years of the baseline period, taken in this study as (1950–1979), while $\text{EPDI}_{\text{future}}$ is the estimate from future period. In the case of CMIP6 projections, the future periods are 20-year long and are shown in Table S1 in Supporting Information S1 for each GWL, model and SSP scenario. The choice of a 20-years period is taken to be consistent with the sixth assessment report of the Intergovernmental Panel on Climate Change (IPCC AR6; IPCC, 2021), in which 20 years is considered to be sufficient for a climate signal to emerge without the influence of natural variability. For assessing observed changes in EPDI from the observational data set HadEX3, $\text{EPDI}_{\text{future}}$ in Equation 2 is taken to be the period (1980–2009), representing the recent past period, while the period for $\text{EPDI}_{\text{hist}}$ is the same as that of CMIP6 models, namely (1950–1979). Moreover, to facilitate comparison between observed and projected changes, we normalize ΔEPDI by warming using the NASA global temperature index data set. Specifically, the average warming between the two periods (1980–2009) and (1950–1979) is 0.42°C, while GWLs of 1.5, 2, 3 and 4°C are converted to 1.29, 1.79, 2.79 and 3.79°C when the baseline period is shifted from pre-industrial to (1950–1979). We divide the values of ΔEPDI by the corresponding warming level to obtain normalized estimates of ΔEPDI per 1 degree C of warming.

While extreme precipitation is often defined by high percentiles, typically at or above the 95th percentile, the specific threshold can vary depending on the definition used (Pendergrass, 2018). Here we chose to define extreme events as those events above the 95th percentile because, in most regions, this criterion encompasses multiple events per year. This approach enhances the signal-to-noise ratio and reduces the sensitivity of our results to outliers. Furthermore, in calculation of EPDI from HadEX3 data set, the denominator in Equation 1 is taken to be total precipitation from days that receive ≥1 mm of precipitation (PRCPTOT) because it is the only available estimate of total precipitation in HadEX3. In contrast, for climate model simulations, we include precipitation amounts below 1 mm. This is because some climate models exhibit a "drizzle effect," whereby precipitation is simulated as more frequent and persistent but less intense, partly due to limitations in convective parameterization schemes (e.g., Chen et al., 2021; Dai, 2006; Trenberth et al., 2003). Including precipitation below 1 mm in the model calculations ensures that EPDI estimates remain conservative and properly account for potential drizzle biases in the simulations.

2.6. Calculating the Change in Rx1day, Annual and Percentile Interval Precipitation Accumulations

To explore how changes in EPDI are related to changes in mean annual precipitation (P) and extreme precipitation (Rx1day), we quantify the changes in both P and Rx1day according to the following equation:

$$\Delta X = \left(\frac{X_{\text{future}} - X_{\text{hits}}}{X_{\text{hist}}}\right) \times 100\% \quad (3)$$

Where X stands for either P or Rx1day for the historical or future periods as defined previously.

Additionally, we also compute the changes in different percentiles of precipitation to gain insights on total changes in the distribution of precipitation (Figure 5 and Figure S5 in Supporting Information S1). For this analysis, values of daily precipitation are extracted for each year separately for the following percentiles: 10th, 20th, 30th, 40th, 50th, 60th, 70th, 80th, 90th and 95th. Percentiles are calculated considering only wet days with precipitation ≥1 mm. Then, the amount of precipitation accumulated between each two consecutive percentiles ([10th−20th[, …, [90th−95th], [95th−AnnualP]) is calculated for both the baseline and future periods. The last step involves taking the climatological average for each percentile interval at both historical and future periods, which are then used to calculate the % change in precipitation amounts using Equation 3.

2.7. Kolmogorov–Smirnov (KS) Test

In order to ensure the statistical significance of the observed changes in EPDI estimated for the period (1980–2009) relative to (1950–1979), we performed a two-sample, two-sided KS test. The two sample KS test is a non-

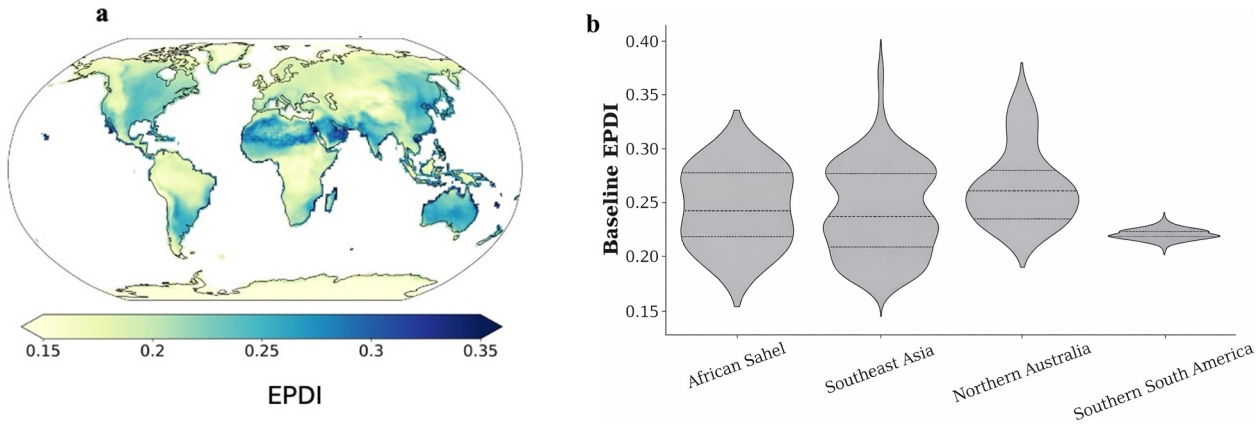

Figure 1. Historical climatology of the Extreme Precipitation Dependency Index (EPDI). (a), Historical climatology of EPDI estimated from a multi-model ensemble mean ($n = 7$) for the period 1950–1979. (b), Distribution of Climatology EPDI values for the 4 IPCC AR6 climate regions with the highest values of EPDI in the period (1950–1979). See Figure S1 in Supporting Information S1 for a map of the IPCC AR6 climate regions.

parametric test that evaluates whether two samples came from the same distribution or not. When performed in its two-sided version, it particularly assesses the null hypothesis (H0) that the two samples are drawn from the same probability distribution. Here, we used the KS test to compare the average values of EPDI from the baseline period (1950–1979) to those from the recent past (1980–2009). For each period, we have a sample size ($n = 3{,}895$), which corresponds to the number of global land grid cells with available observations from HadEX3 (see Figure S3 in Supporting Information S1). Our results show that the null hypothesis can be rejected with a p-value of 1.5 e−16. In other words, the two samples are different at a statistical significance level <<0.00001. The sign of the test statistic also indicates that the distribution of EPDI at (1980–2009) is higher than that of the period (1950–1979).

3. Results

3.1. Historical Climate EPDI

The map in Figure 1a shows the EPDI, estimated from a multi-model ensemble mean for the period (1950–1979). Over global land, EPDI for the period (1950–1979) ranged from 0.07 (5th percentile) to 0.28 (95th percentile). The highest values of EPDI are in the African Sahel, the Asian-Australian monsoon regions, the Arabian Peninsula and the southern part of South America as shown in Figure 1b (the exact boundaries of these regions are shown in Figure S1 in Supporting Information S1). In some of these regions, over one fourth of annual precipitation falls within the wettest 5% of days. Results from individual models Figures S2a–S2g in Supporting Information S1) show similar spatial patterns to those of the multi-model ensemble mean apart from overestimation biases at the Sahara for some models, which can be attributed to sensitivity of the results to the low precipitation amounts in the region. Some of the biases observed in individual models may stem from biases in the models' precipitation data itself. For example, the drizzle effect—where precipitation is simulated as more frequent and prolonged but less intense—can arise from limitations in convective parameterization schemes (Chen et al., 2021; Dai, 2006; Trenberth et al., 2003). Overall, both the individual models and their ensemble mean show appropriate resemblance to the observed spatial patterns from HadEX3 for the same time period (1950–1979), shown in Figure S2h in Supporting Information S1. This indicates that the multi-model ensemble may be used to examine projected changes and spatial patterns of EPDI. It should be noted that in this study, we compared each model's projected EPDI values with the historical values estimated by the same model, thereby reducing the influence of systematic biases in the model's precipitation data.

3.2. Projected Changes in EPDI

Figure 2 shows the projected changes in EPDI at different GWLs. At +1.5 and +2°C warming, EPDI increases over all global land with an average rate of 3.8% and 5.4%, respectively. At regional scales, the increase in EPDI is mostly moderate with 88% and 82% of grid cells experiencing an increase of less than 5% for warming levels of both +1.5 and +2°C. There are a few exceptions with increases above 10% in the Sahara, Greenland, and the

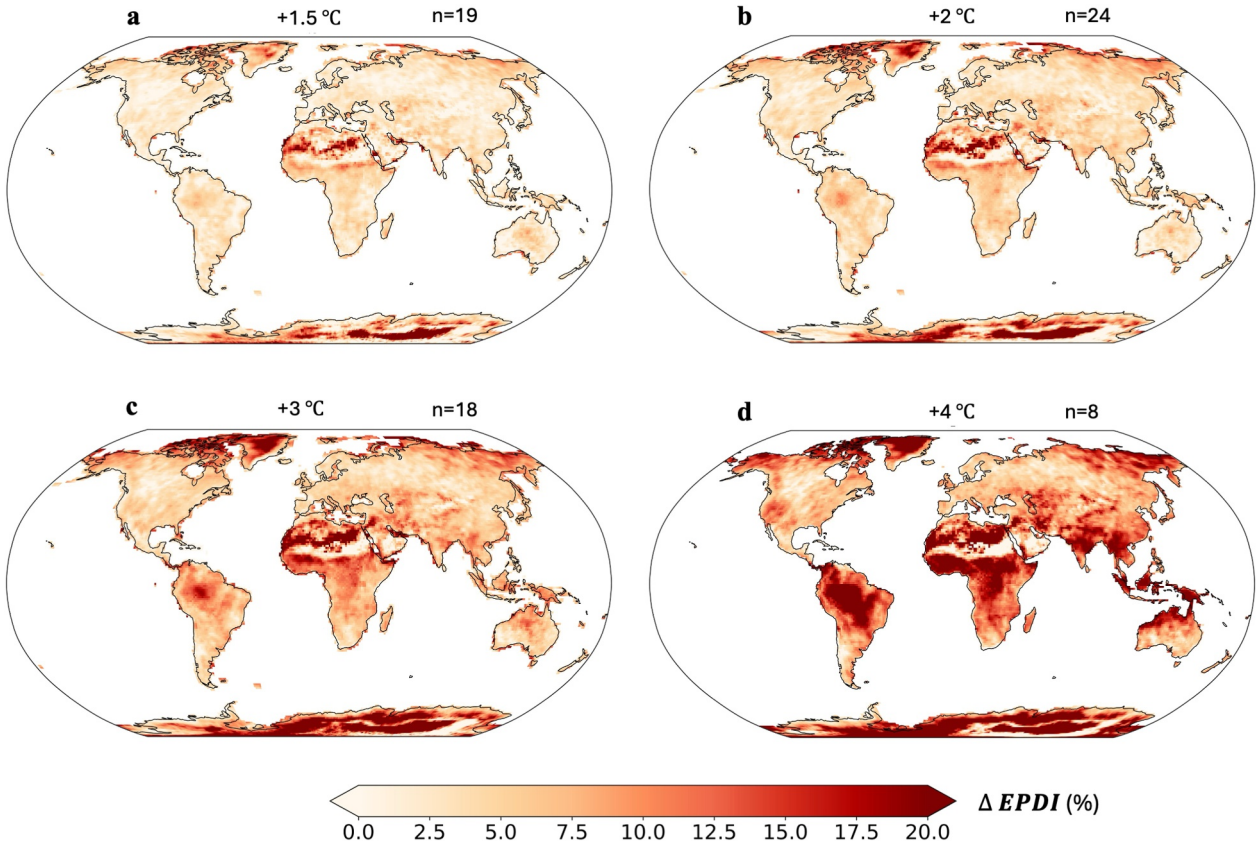

Figure 2. Changes in the Extreme Precipitation Dependency Index (EPDI). (a), Multi-model ensemble mean percent change in EPDI at global warming level of +1.5°C. (b), Same as a, but for +2°C. (c), Same as a, but for +3°C. (d), Same as a, but for +4°C. Warming levels are calculated relative to the period 1850–1900, while the change in precipitation is calculated relative to the period 1950–1979. In panels (a–d), *n* indicates the number of models used in the calculation.

Arctic, which can mostly be attributed to the hyper-arid nature of these regions. That is, the calculated changes in precipitation can be very sensitive to the low values of precipitation in present climate (Ombadi et al., 2023). Conversely, at higher warming levels of +3 and +4°C, a sharp increase in EPDI is projected over large portions of global land, particularly over the African Sahel, Central and Southern Africa, South America, India and Northern Australia. For comparison, we also calculated changes in EPDI from the observational data set HadEX3 for the period (1980–2009) relative to the baseline period (1950–1979). The results, shown in Supporting Information S1 Figure S3, demonstrate that in 64% of global land regions where HadEX3 observations are available, there has been an increase in the fraction of extremes to annual precipitation, with EPDI increasing by more than 10% in some regions (26% of grid cells with available HadEX3 observations). The observed changes are statistically significant according to a two-sided KS test (p-value <0.001; see Methods for more details).

To understand how changes in EPDI are shaped by different trends in annual and extreme precipitation, Figure 3 shows the joint distribution of relative changes in annual precipitation (ΔP ; x-axis) and extreme daily precipitation (ΔRx1day; y-axis) at each GWL, overlapped with the corresponding changes in the EPDI. The horizontal and vertical dashed black lines in Figure 3 show zero change in ΔRx1day and ΔP , respectively, offering reference axes to delineate quadrants of increasing or decreasing annual precipitation and extremes. Each data point in Figure 3 presents a specific grid point over the spatial domain of global land. Overall, the majority of grid points are either located in the 1st-quadrant ($\Delta P > 0$ and ΔRx1day > 0) or the 2nd-quadrant ($\Delta P < 0$ and ΔRx1day > 0). This is consistent with the general trends in annual and extreme precipitation shown in Figure S4 (Supporting Information S1). As shown in Figure 3, the high ΔEPDI values (dark colors) are located in the first quadrant above the 1:1 line, indicating that both annual and extreme precipitation are increasing, with extremes increasing at a faster rate than annual totals. Additionally, grid points located in the 2nd-quadrant also exhibit a high change in EPDI with values in the range of 10%–20%. These are regions where extreme precipitation is intensifying, but annual precipitation is decreasing. The combined effect of these changes result in an increased

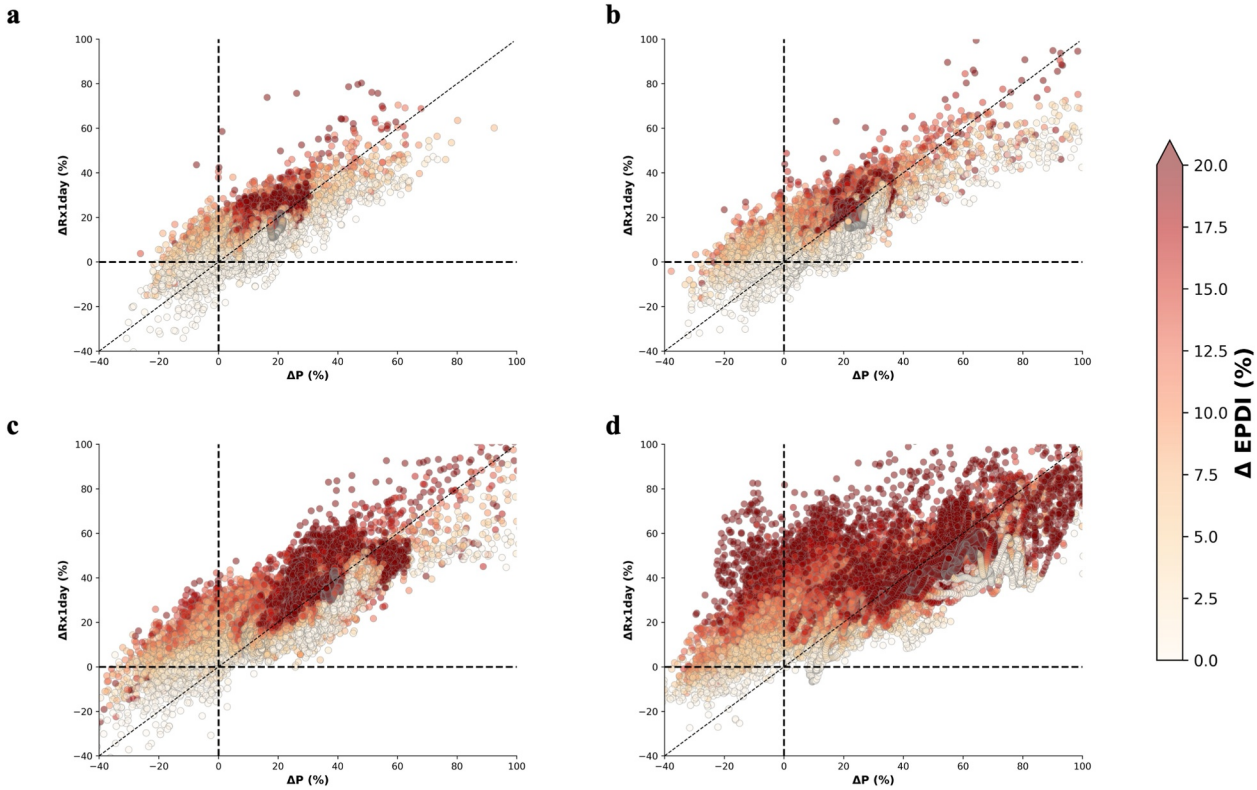

Figure 3. Joint distribution of percentage changes in annual precipitation (Δ*P*), horizontal axis, and extreme daily precipitation (ΔRx1day), vertical axis, colored by changes in the Extreme Precipitation Dependency Index (ΔEPDI), obtained from the multi-model ensemble mean. (a), at global warming level (GWL) of +1.5°C. (b), at GWL of +2°C. (c), at GWL of +3°C. (d), at GWL of +4°C. Warming levels are calculated relative to the period 1850–1900, while the change in precipitation is calculated relative to the period 1950–1979.

dependency on daily extreme precipitation. Maps of projected changes in annual precipitation (Figure S4a–S4d; in Supporting Information S1) reveal that the regions where annual precipitation, P, decreases are the Mediterranean, Southern Africa and parts of South America and Australia, which is consistent with the projected decline in subtropical precipitation (He & Soden, 2016; Neelin et al., 2006).

Furthermore, it can also be seen from Figure 3 that with the increase in GWL (from 1.5°C to 4°C), more grid points are located in the 1st and 2nd quadrants, while also exhibiting higher changes in EPDI (dark red colors). This is because at higher GWLs, the amplitude of projected changes in different regions of the globe intensifies (see maps in Figure S4; in Supporting Information S1). More specifically, the mean percentage increase in *P* over global land is 7.1%, 11.4%, 18% and 30.7% for warming levels of +1.5, +2, +3 and +4°C, respectively. Similarly, the projected increases in Rx1day also strengthen with warming, with global land mean of 9.6%, 14.1%, 22.8% and 37.1% for warming levels of +1.5, +2, +3 and +4°C. Note that in the present study, all analysis of change in precipitation is carried out relative to the baseline period (1950–1979), while GWLs are assessed relative to (1850–1900) in accordance with IPCC definitions.

3.3. Regional Hotspots

In order to further examine the regional changes in EPDI, we carried out an analysis of the projected changes using the IPCC climate reference regions (Iturbide et al., 2020). Figure 4a shows the distribution of area-weighted average change in EPDI under different GWLs, with each data point corresponding to one of the 44 IPCC climate regions used in this study (see Methods). The interquartile range (25th–75th percentiles) is below 5% for both 1.5 and 2°C warming, with only 4 and 11 regions experiencing an increase above 5%, respectively. At +3°C, however, 31 regions (70%) are projected to experience an increase in EPDI of more than 5%. Note that GWLs are calculated relative to (1850–1900), and we are already at approximately 1.1°C warming. These robust changes in the EPDI are even more evident at +4°C with almost all of the 44 regions (95%) showing an increase above 5%.

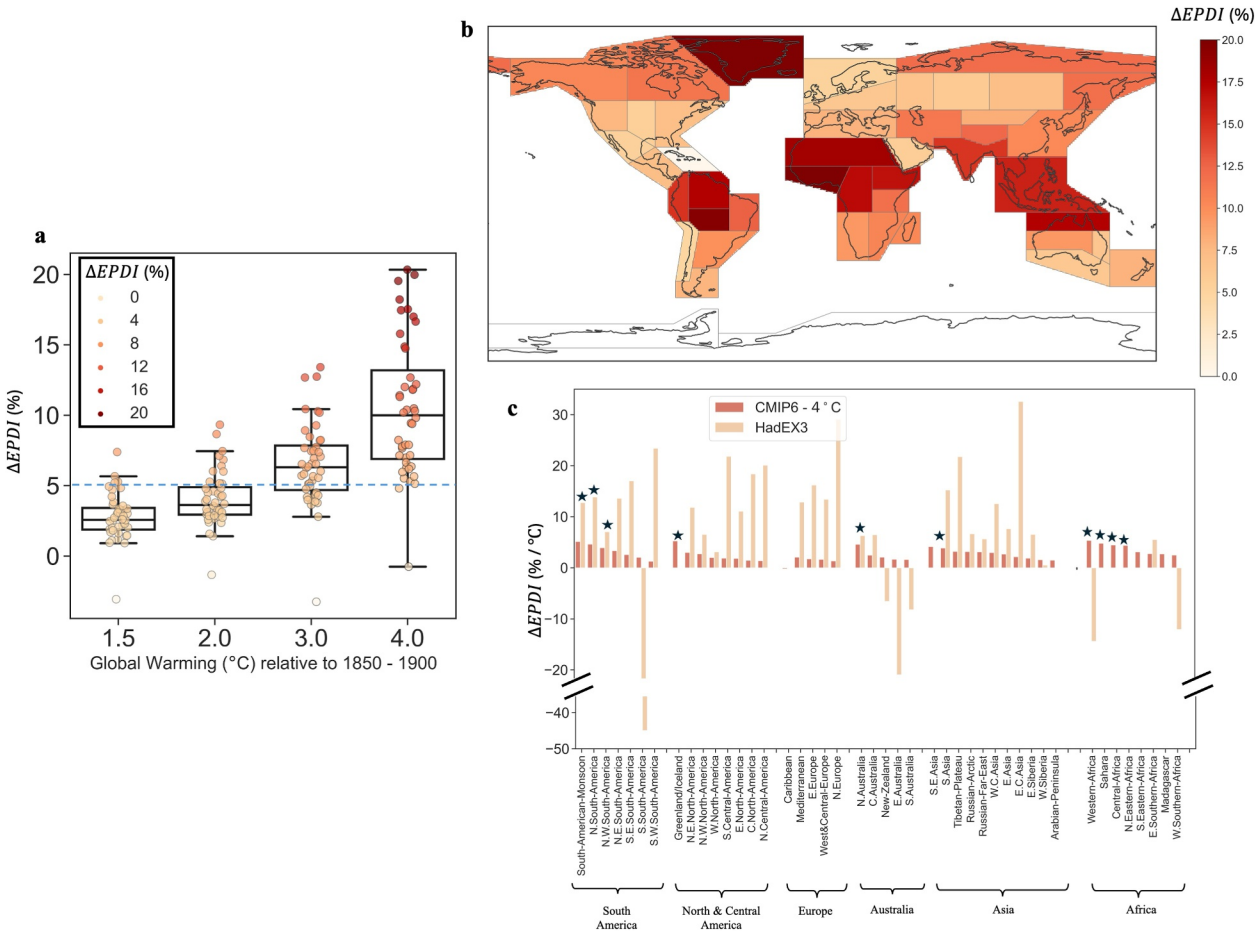

Figure 4. Regional analysis of changes in the fraction of extremes. (a), Multi-model ensemble mean percentage change in the fraction of extremes to annual precipitation (Extreme Precipitation Dependency Index (EPDI)), averaged across IPCC AR6 climate regions and expressed as a function of global warming levels of +1.5, +2, +3, and +4°C. The boxes show the interquartile range (IQR; 25th to 75th percentiles) and the whiskers show the extent of the distribution excluding outliers, defined as values greater than (75th percentile +1.5*IQR) or lower than (25th percentile − 1.5*IQR). (b), The area-weighted average of the percentage change in the fraction of extremes at 4°C warming across the 44 IPCC AR6 climate regions. (c), The percentage changes in EPDI from the +4°C Coupled Model Intercomparison Project ensemble (dark color) compared to the observed changes in HadEX3 data set for the period 1980–2009 relative to 1950–1979 (light color). In (c), climate regions are grouped for each continent and ranked from highest to lowest projected change in EPDI. Asterisk symbol indicate regions where the projected change in EPDI is equal to or greater than 15%.

These +4°C results are further analyzed to identify regional hotspots that are likely to experience substantial increases in the fraction of extremes to annual precipitation. Figures 4b and 4c clearly demonstrate that the South-American Monsoon region, Northern South America, Northern Australia, Southeast Asia, Western Africa, Northeastern Africa, Central Africa and the Sahara are all regional hotspots with projected change in EPDI of 15% or higher.

Figure 4c also shows the observed changes in EPDI estimated from HadEX3 for the period (1980–2009) relative to (1950–1979), and averaged over IPCC climate regions. To facilitate comparison between observed and projected changes in EPDI, we normalize ΔEPDI by the associated warming (in °C; see Methods). Overall, observations indicate increasing EPDI across most regional hotspots, with the exception of Western Africa, where EPDI has decreased over the past few decades. Notably, the observed rate of EPDI increase exceeds that projected by climate models, potentially suggesting that models underestimate changes in EPDI. While projections consistently show increases in EPDI across all regions, observations reveal decreases in a few regions, including southern South America, southern Australia, eastern Australia, and Western Africa. This is very likely due to a low signal-to-noise ratio in the observational record. Specifically, in the analysis shown in Figure 4c, we calculate changes in EPDI for the period 1980–2009 relative to the baseline period 1950–1979. Over this interval, the increase in mean global surface temperature is approximately 0.42°C (based on NASA global temperature index

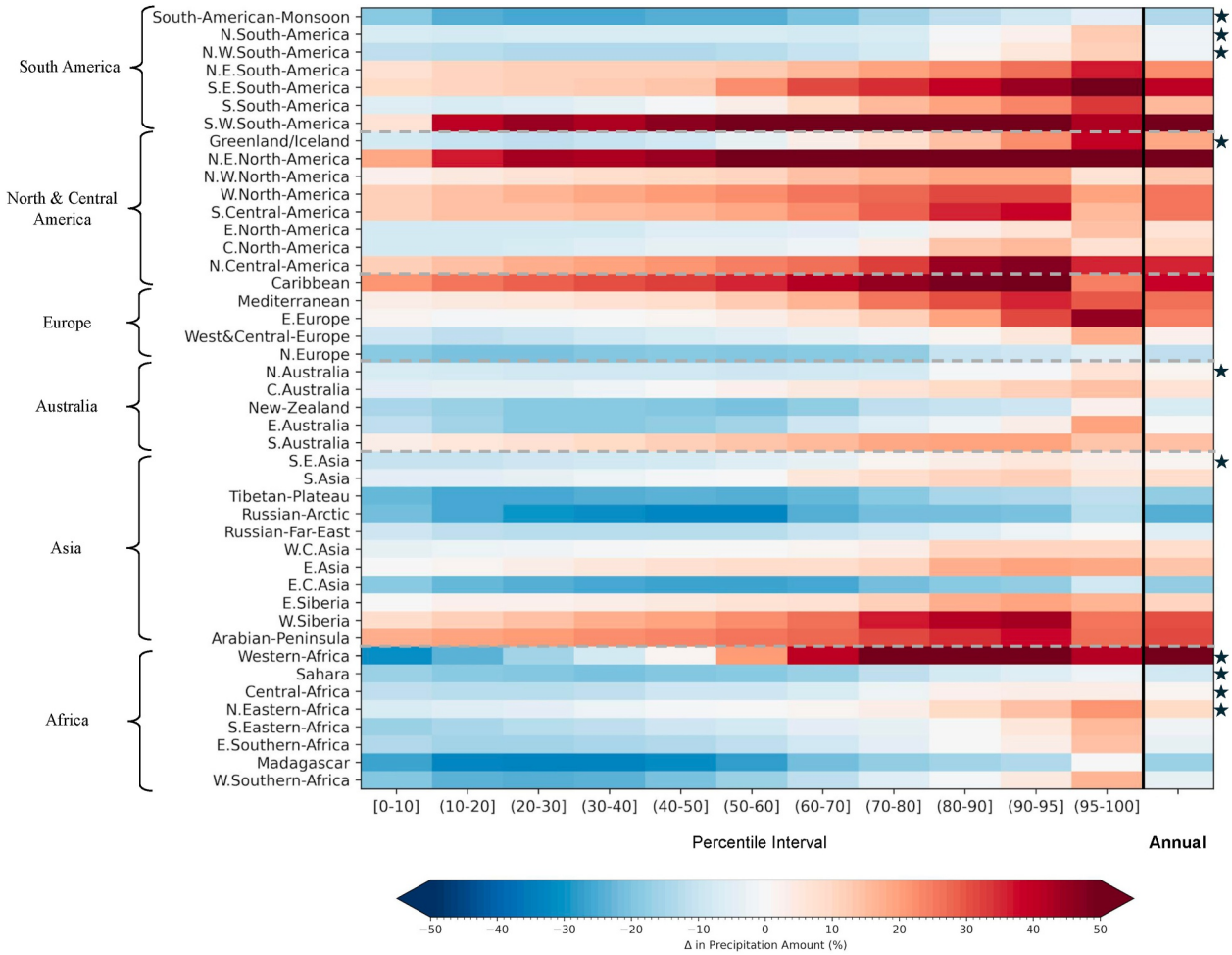

Figure 5. Projected changes in the distribution of daily precipitation. Multi-model ensemble mean projected changes in the amount of daily precipitation accumulated at the following percentile intervals [0–10], (10–20], (20–30], (30–40], (40–50], (50–60], (60–70], (70,80], (80–90], (90–95], (95–100]. Projected changes are computed for global warming level of 4°C relative to the historical period (1950–1979), and averaged over IPCC climate regions. The heatmap also shows projected changes in annual precipitation. The IPCC regions are grouped into continents and ordered from top to bottom based on the values of ΔEPDI, with the asterisk symbol denoting regional hotspots with ΔEPDI ≥ 15%.

data), which is substantially smaller than the warming projected for the 21st century. Consequently, EPDI variability in the observations is more strongly influenced by natural climate variability, resulting in greater noise and a weaker emerging signal attributable to warming.

3.4. Changes in the Distribution of Precipitation

In order to understand how the increase in EPDI relates to overall changes in the distribution of daily precipitation, Figure 5 shows the projected change in precipitation amounts accumulated in percentile intervals of [0–10], (10–20] (80–90], (90–95] and (95–100] at 4°C warming relative to the baseline period of (1950–1979), and averaged over IPCC climate regions. The figure also shows projected changes in annual precipitation (rightmost column). It is clear that across all climate regions, there is a robust gradient in the change of precipitation amounts, with decreases (blue color) in low percentile intervals and increases (red color) in high percentile intervals. In particular, the change in precipitation amounts in the percentile interval (95–100], which is used for calculating EPDI, is almost exclusively increasing across all regions. These patterns show that the amount of precipitation from extreme events is expected to become larger, while that of moderate and light events will become smaller. In other words, instead of all precipitation types getting heavier, only extreme events will see a significant increase in intensity, while others are expected to decrease in intensity. Similar conclusions can be obtained from the analysis conducted at 1.5, 2 and 3°C warming, which is shown in Figure S5 (Supporting Information S1). It can also be

seen from Figure 5 that in several regions, the projected increase in precipitation amounts within high percentile intervals is associated with a projected decrease in annual precipitation. This pattern is most evident in regional hotspots (indicated with an asterisk in the figure), and it means that in those regions annual precipitation is not just declining but is also coming within fewer days in the year. Such projected changes are alarming and bear significant implications for rain-fed agriculture and water resources management, which we discuss in the next section.

3.5. Quantifying Impacts on Rain-Fed Agriculture

We have shown strong patterns of past and predicted changes in EPDI globally, which give rise to the question: what might the impacts be and why should they matter, specifically for water resources, agriculture and natural ecosystems? We argue that EPDI is important for several reasons, because (in concert with total P) it provides a more complete metric that is diagnostic of multiple impacts of precipitation than extreme or annual precipitation alone, and equally important, because those multiple impacts are more varied, complex and nuanced than often perceived. For agricultural systems, changes in EPDI are arguably as important as changes in either annual or extreme precipitation. For instance, agricultural yield is sensitive to the distribution, relative frequency, and total volume of heavy, moderate and low precipitation events. Specifically, it has been shown that heavy precipitation reduces crop yield and causes agricultural damages (Rosenzweig et al., 2002; Vogel et al., 2019; Zhu & Troy, 2018), while other studies revealed a complex relationship in which crop yield benefits from increases in extreme precipitation up to a certain threshold beyond which reductions in yield are expected (Lesk et al., 2020). While changes in precipitation regimes can affect both irrigated and rain-fed agriculture, the impacts on the latter are more substantial because crop growth depends solely on the amount and spatio-temporal distribution of precipitation. Here, we use a high resolution Landsat-derived data set (Teluguntla et al., 2023), that maps the global agricultural land into irrigated and rain-fed croplands, to estimate the percentage of global rain-fed agricultural land that is likely to experience large increases in EPDI in a warmer climate.

The bar chart in Figure 6 shows the percentage of global rain-fed agricultural land that is projected to experience a change in EPDI of 5% or more. At 1.5 and 2°C warming, only 4% and 15% of global rain-fed cropland is projected to experience an increase of 5%–10% in EPDI. When compared to warming levels beyond the UN mitigation targets, namely 3 and 4°C, the affected area of rain-fed cropland increases sharply to 54% and 96%, respectively. Even more concerning is that under such warming levels, a sizable percentage of rain-fed cropland is projected to experience an increase in EPDI of 10%–20%. These results underscore the importance of limiting warming in accord with the Paris Agreement thresholds to avoid exposure of rain-fed agriculture to such changes. The spatial distribution of the affected rain-fed cropland differs depending on warming level and the range of change in EPDI as shown in the pie charts in Figure 6 and the maps in Figure 7 (aggregated at AR6 regions) and Figure S6 in Supporting Information S1 (at grid scale). Overall, it can be clearly seen that Africa, Asia and South America are the three continents that constitute the majority of the affected rain-fed cropland. Additionally, Figure 7 shows that as warming changes from 3 to 4°C, there is both an intensification of EPDI changes in affected areas as well as an emergence of new areas. Given that rain-fed agriculture is most prevalent in low-income and developing countries such as those in Sub-Saharan Africa, India and South America, our findings suggest that global warming is likely to increase exposure of changes in precipitation regimes in an already vulnerable region. Therefore, we argue that it is important to incorporate these results into local climate change adaptation efforts in developing countries.

4. Discussion

4.1. Implications for Water Resources Management

In addition to potential impacts on rain-fed agriculture, the projected increase in EPDI bears significant implications for water resources management. A higher fraction of annual precipitation falling within extreme events poses significant challenges to reservoir management, since reservoirs are operated to release water downstream, as opposed to storing water, during heavy downpours. This process is known as flood hedging which optimally determines the amount of released water needed to increase the reservoir storage capacity, which in turn, is utilized for flood control (Draper & Lund, 2004; Zhao et al., 2014). Because of flood hedging, only a fraction of the water falling within extreme events can be captured; thus, an increased fraction of annual precipitation falling within extreme events can significantly undermine water availability in a warmer climate.

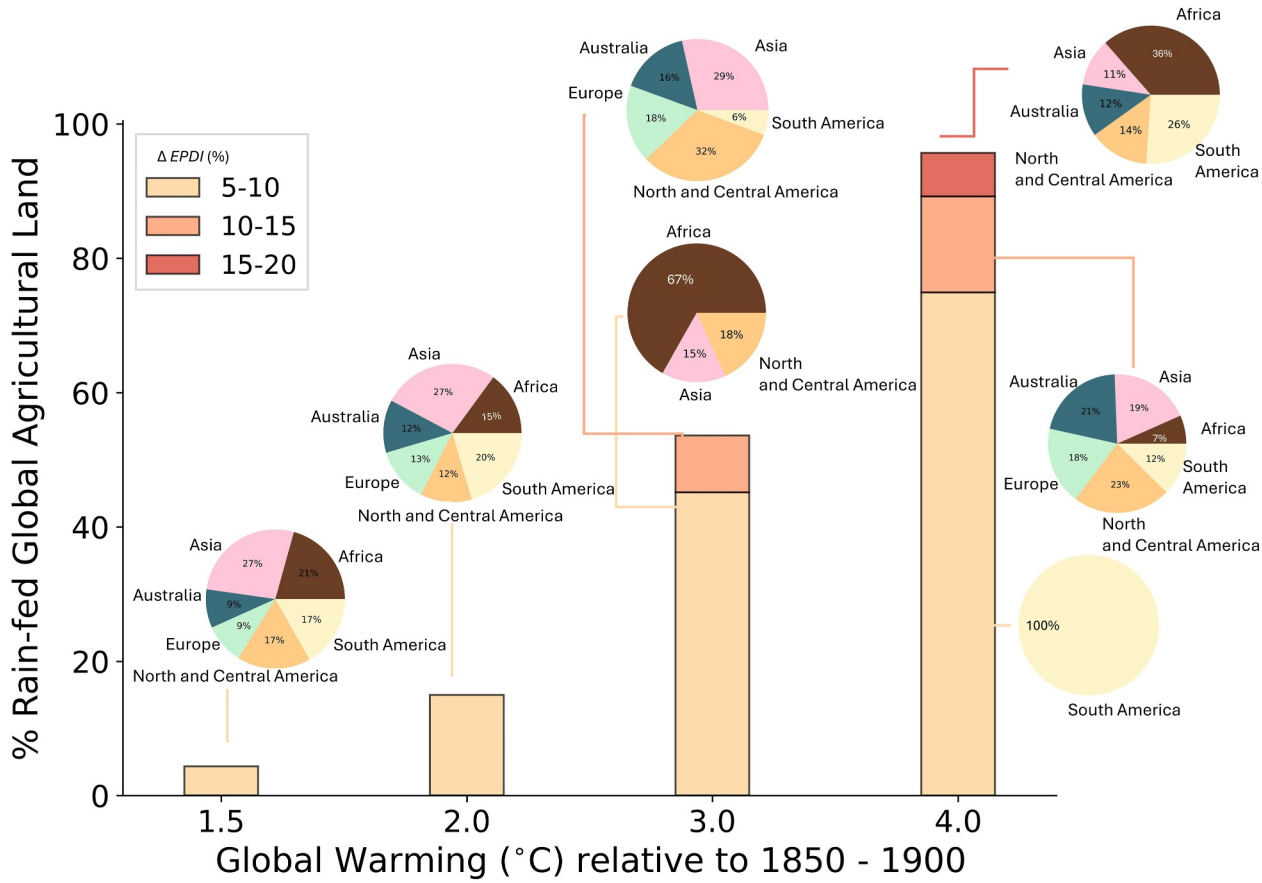

Figure 6. Exposure of global rain-fed agricultural land to changes in the Extreme Precipitation Dependency Index (EPDI). Stacked bar chart shows the percentage of global rain-fed agricultural land subjected to changes in EPDI, ΔEPDI, in the range of (5%–10%), (10%–15%) and (15%–20%) at global warming levels (GWLs) of 1.5, 2, 3 and 4°C. At each GWL and range of ΔEPDI, the pie charts show the distribution of the rain-fed cropland across the six continents: Africa, Asia, Europe, South America, North and Central America, and Australia.

4.2. Implications for Ecosystems Functioning

Furthermore, increased fraction of annual precipitation as extreme events will have multiple cascading impacts on natural ecosystems, including forests and grasslands. For example, a greater EPDI with a similar or even a slightly higher annual precipitation will mean more rain falling in heavy events with lesser recharge and more run-off; longer dry periods between rain events, during which soil moisture deficits will grow larger and be longer; in addition, some of those rain events will by default be smaller and thus provide less recharge. In many temperate and boreal forests, these effects will be compounded (Y. Wang et al., 2014) by the fact that more of the precipitation will fall earlier in the growing season (Seager et al., 2014), meaning less soil moisture available in mid-summer when Potential Evapotranspiration (PET) is highest, and growing higher by the decade with increased temperatures and vapor pressure deficit (VPD). These changes will likely be particularly profound for boreal forests which operate nearer to the frontier between sufficient and insufficient moisture than temperate and tropical forests (Liu et al., 2020) and have suffered significant impacts directly (e.g., drought) and indirectly (wildfire); thus we will focus on this example herein.

In boreal forests, an increasing EPDI is problematic when viewed within the context of typical seasonal precipitation distribution. Although boreal forests occur in cool regions, low P, relative to PET, means they operate closer to water shortage than temperate and tropical forests and often suffer mid-late summer water shortages, as the ratio of PET to *P* is highest during that season (Liu et al., 2020; J. A. Wang et al., 2021). Given evidence that increasing extreme events represent an increasing fraction of P, increasing EPDI means lesser rain amounts during non-extreme events, greater time lengths between rain events, or both; the former is likely to also result in lesser recharge from a given event due to a greater proportion of canopy evaporation. As the ratio of precipitation

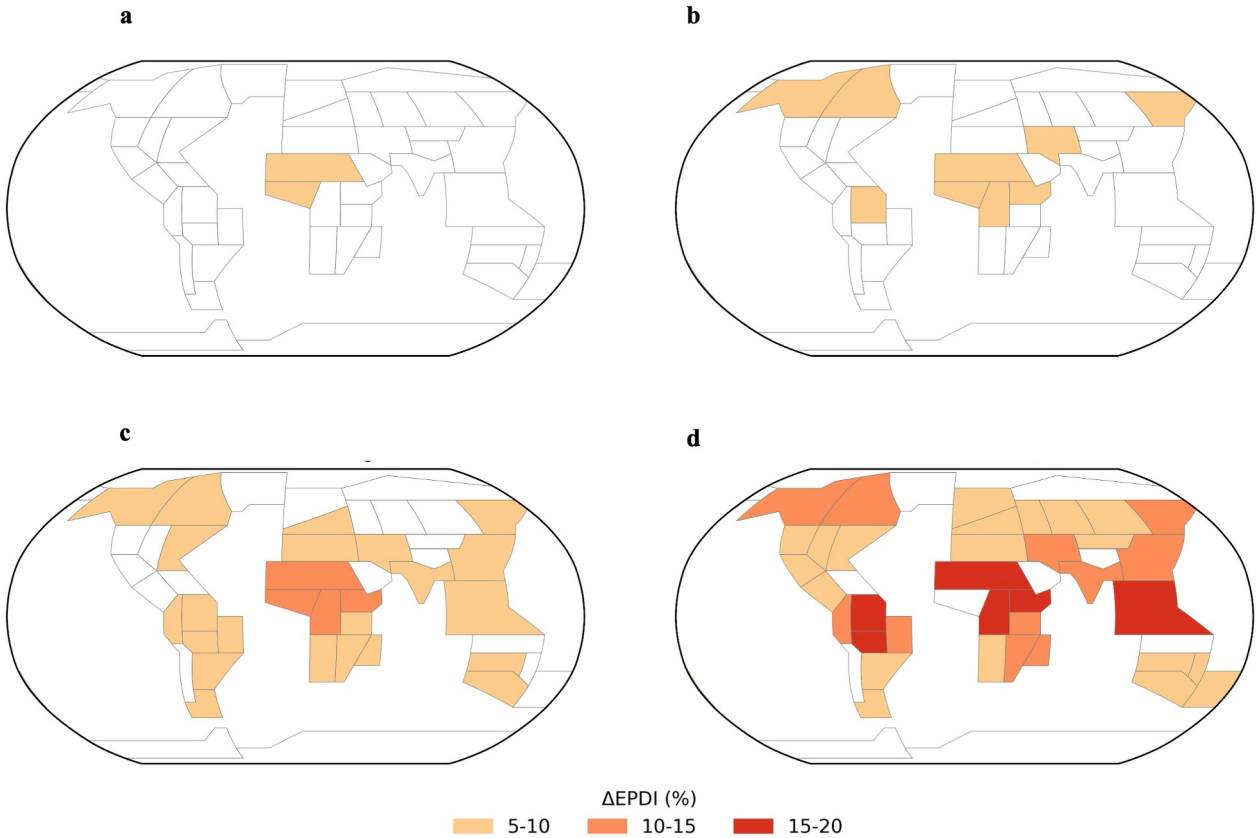

Figure 7. Area-weighted average change in the Extreme Precipitation Dependency Index (EPDI) for Global Warming Levels of: (a) 1.5°C, (b) 2°C, (c) 3°C and (d) 4°C. Color coding show the change in EPDI, ΔEPDI, for values in the range of (5%–10%), (10%–15%) and (15%–20%). All values are calculated at the scale of the 44 IPCC AR6 climate.

to PET is higher in spring and early summer, and decreases in mid-late summer when PET is highest (Liu et al., 2020; Seager et al., 2014), increasing EPDI is likely to further exacerbate the tendency for summer dry spells to be longer and drier, and to occur in concert with higher VPD (Mirabel et al., 2023; Seager et al., 2014), leading to reduced photosynthesis, growth and survival of both mature trees and their replacement regeneration (Ma et al., 2012; Mirabel et al., 2023; Peng et al., 2011; Reich et al., 2018, 2022). Additionally, for the same reason that increased EPDI adversely influences boreal forest growth and survival, it likely contributes to rapid increase in the frequency, magnitude and spatial extent of wildfires (Barnes et al., 2023).

5. Conclusions

In the present paper, we demonstrated, according to model projections, that EPDI will increase considerably over most global land regions, with far-reaching implications on food production, forests and water resources management. Those impacts are largely distinct from those of extreme precipitation, and they necessitate building societal resilience through adaptive design of agricultural and reservoir operation systems. For instance, rainwater harvesting techniques (Helmreich & Horn, 2009; Pandey et al., 2003) can play a major role in alleviating the potential impacts of an increasing EPDI, as they enable capturing water during storms and redistributing it through both time and space. Similarly, multi-objective reservoir operation rules (Huang et al., 2019) and improved use of weather forecasts (Nayak et al., 2018) is crucial to effectively manage water resources when most of the water comes from extreme events. Our findings also provide a cogent argument for the importance of limiting global warming to the Paris Agreement goals of 1.5–2°C above pre-industrial levels, since the exposure to the increase in the EPDI increases sharply beyond those targets. Lastly, it is important to emphasize that our observations-based estimates of the change in the EPDI are higher than those obtained from climate model projection, and they suggest that climate models may be underestimating these changes. This opens new research

avenues on reconciling the different rates of increase between models and observations, and potentially pinpointing key areas of model improvement.

Conflict of Interest

The authors declare no conflicts of interest relevant to this study.

Availability Statement

The precipitation data is available from the CMIP6 Phase 6 (CMIP6): https://esgf-node.ipsl.upmc.fr/projects/cmip6-ipsl (accessed on 09-20-2025). Precipitation observations can be accessed from the Gridded Land Surface Extremes Indices (HadEX3): https://www.metoffice.gov.uk/hadobs/hadex3/ (accessed on 09-20-2025). The Landsat-Derived Global Rainfed and Irrigated-Cropland Product 30 m V001 (LGRIP30) satellite data can be downloaded from: (Teluguntla et al., 2023). NASA Global Temperature Index data set is available at https://science.nasa.gov/earth/explore/earth-indicators/global-temperature/ (accessed on 01-21-2025). The codes and post-processed data needed to reproduce the results presented in this article are deposited in Figshare at https://doi.org/10.6084/m9.figshare.31220725.v1 (Ombadi, 2026).

Acknowledgments
This research was supported by startup funds provided through the Department of Climate and Space Science and Engineering and the College of Engineering at the University of Michigan for M. Ombadi. We thank the World Climate Research Programme and the climate modeling groups for producing and making their model output publicly available for researchers.

References

Allen, M. R., & Ingram, W. J. (2002). Constraints on future changes in climate and the hydrologic cycle. *Nature*, *419*(6903), 224–232. https://doi.org/10.1038/nature01092

Alter, R. E., Im, E.-S., & Eltahir, E. A. B. (2015). Rainfall consistently enhanced around the Gezira scheme in East Africa due to irrigation. *Nature Geoscience*, *8*(10), 763–767. https://doi.org/10.1038/ngeo2514

Asadieh, B., & Krakauer, N. Y. (2015). Global trends in extreme precipitation: Climate models versus observations. *Hydrology and Earth System Sciences*, *19*(2), 877–891. https://doi.org/10.5194/hess-19-877-2015

Ayat, H., Evans, J. P., Sherwood, S. C., & Soderholm, J. (2022). Intensification of subhourly heavy rainfall. *Science*, *378*(6620), 655–659. https://doi.org/10.1126/science.abn8657

Bao, J., Sherwood, S. C., Alexander, L. V., & Evans, J. P. (2017). Future increases in extreme precipitation exceed observed scaling rates. *Nature Climate Change*, *7*(2), 128–132. https://doi.org/10.1038/nclimate3201

Barnes, C., Boulanger, Y., Keeping, T., Gachon, P., Gillett, N., Haas, O., et al. (2023). Climate change more than doubled the likelihood of extreme fire weather conditions in eastern Canada.

Calvin, K., Dasgupta, D., Krinner, G., Mukherji, A., Thorne, P. W., Trisos, C., et al. (2023). In h. lee, j. romero, P. Arias, et al. (Eds.) *Ipcc, 2023: Climate change 2023: Synthesis report. Contribution of working groups I, ii and iii to the sixth assessment report of the intergovernmental panel on climate change [core writing team*. https://doi.org/10.59327/ipcc/ar6-9789291691647

Chen, D., Dai, A., & Hall, A. (2021). The convective-to-total precipitation ratio and the "drizzling" bias in climate models. *Journal of Geophysical Research: Atmospheres*, *126*(16), e2020JD034198. https://doi.org/10.1029/2020jd034198

Chen, G., Norris, J., Neelin, J. D., Lu, J., Leung, L. R., & Sakaguchi, K. (2019). Thermodynamic and dynamic mechanisms for hydrological cycle intensification over the full probability distribution of precipitation events. *Journal of the Atmospheric Sciences*, *76*(2), 497–516. https://doi.org/10.1175/jas-d-18-0067.1

Dai, A. (2006). Precipitation characteristics in eighteen coupled climate models. *Journal of Climate*, *19*(18), 4605–4630. https://doi.org/10.1175/jcli3884.1

Dai, A. (2021). Hydroclimatic trends during 1950–2018 over global land. *Climate Dynamics*, *56*(11–12), 4027–4049. https://doi.org/10.1007/s00382-021-05684-1

Dollan, I. J., Maggioni, V., & Johnston, J. (2022). Investigating temporal and spatial precipitation patterns in the southern mid-atlantic United States. *Frontiers in Climate*, *3*, 799055. https://doi.org/10.3389/fclim.2021.799055

Donat, M. G., Lowry, A. L., Alexander, L. V., O'Gorman, P. A., & Maher, N. (2016). More extreme precipitation in the world's dry and wet regions. *Nature Climate Change*, *6*(5), 508–513. https://doi.org/10.1038/nclimate2941

Douville, H., Raghavan, K., Renwick, J., Allan, R. P., Arias, P. A., Barlow, M., et al. (2021). Water cycle changes.

Draper, A. J., & Lund, J. R. (2004). Optimal hedging and carryover storage value. *Journal of Water Resources Planning and Management*, *130*(1), 83–87. https://doi.org/10.1061/(asce)0733-9496(2004)130:1(83)

Dunn, R. J., Alexander, L. V., Donat, M. G., Zhang, X., Bador, M., Herold, N., et al. (2020). Development of an updated global land in situ-based data set of temperature and precipitation extremes: Hadex3. *Journal of Geophysical Research: Atmospheres*, *125*(16), e2019JD032263. https://doi.org/10.1029/2019jd032263

Dunn, R. J., Donat, M. G., & Alexander, L. V. (2022). Comparing extremes indices in recent observational and reanalysis products. *Frontiers in Climate*, *4*, 989505. https://doi.org/10.3389/fclim.2022.989505

Eyring, V., Bony, S., Meehl, G. A., Senior, C. A., Stevens, B., Stouffer, R. J., & Taylor, K. E. (2016). Overview of the coupled model intercomparison project phase 6 (cmip6) experimental design and organization. *Geoscientific Model Development*, *9*(5), 1937–1958. https://doi.org/10.5194/gmd-9-1937-2016

Hauser, M., Engelbrecht, F., & Fischer, E. M. (2022). Transient global warming levels for CMIP5 and CMIP6. *Zenodo*. https://doi.org/10.5281/ZENODO.7390473

Hauser, M., Spring, A., & Busecke, J. (2016). Regionmask: Plotting and creation of masks of spatial regions. Retrieved from https://regionmask.readthedocs.io/en/stable/index.html

He, J., & Soden, B. J. (2016). A re-examination of the projected subtropical precipitation decline. *Nature Climate Change*, *7*(1), 53–57. https://doi.org/10.1038/nclimate3157

Helmreich, B., & Horn, H. (2009). Opportunities in rainwater harvesting. *Desalination*, *248*(1–3), 118–124. https://doi.org/10.1016/j.desal.2008.05.046

Huang, L., Li, X., Fang, H., Yin, D., Si, Y., Wei, J., et al. (2019). Balancing social, economic and ecological benefits of reservoir operation during the flood season: A case study of the three gorges project, China. *Journal of Hydrology*, *572*, 422–434. https://doi.org/10.1016/j.jhydrol.2019.03.009

IPCC. (2021) In V. Masson-Delmotte, P. Zhai, A. Pirani, S. L. Connors, C. Péan, et al. (Eds.) *Climate change 2021: The physical science basis. Contribution of working group I to the sixth assessment report of the intergovernmental panel on climate change*. Cambridge Univ. Press. https://doi.org/10.1017/9781009157896

Iturbide, M., Gutierrez, J. M., Alves, L. M., Bedia, J., Cerezo-Mota, R., Cimadevilla, E., et al. (2020). An update of ipcc climate reference regions for subcontinental analysis of climate model data: Definition and aggregated datasets. *Earth System Science Data*, *12*(4), 2959–2970. https://doi.org/10.5194/essd-12-2959-2020

Karl, T. R., & Knight, R. W. (1998). Secular trends of precipitation amount, frequency, and intensity in the United States. *Bulletin of the American Meteorological Society*, *79*(2), 231–241. https://doi.org/10.1175/1520-0477(1998)079⟨0231:stopaf⟩2.0.co;2

Lesk, C., Coffel, E., & Horton, R. (2020). Net benefits to Us soy and maize yields from intensifying hourly rainfall. *Nature Climate Change*, *10*(9), 819–822. https://doi.org/10.1038/s41558-020-0830-0

Liu, J., Cheng, F., Munger, W., Jiang, P., Whitby, T. G., Chen, S., & Man, X. (2020). Precipitation extremes influence patterns and partitioning of evapotranspiration and transpiration in a deciduous boreal larch forest. *Agricultural and Forest Meteorology*, *287*, 107936. https://doi.org/10.1016/j.agrformet.2020.107936

Ma, Z., Peng, C., Zhu, Q., Chen, H., Yu, G., Li, W., et al. (2012). Regional drought-induced reduction in the biomass carbon sink of canada's boreal forests. *Proceedings of the National Academy of Sciences*, *109*(7), 2423–2427. https://doi.org/10.1073/pnas.1111576109

Mirabel, A., Girardin, M. P., Metsaranta, J., Way, D., & Reich, P. B. (2023). Increasing atmospheric dryness reduces boreal forest tree growth. *Nature Communications*, *14*(1), 6901. https://doi.org/10.1038/s41467-023-42466-1

Nayak, M. A., Herman, J. D., & Steinschneider, S. (2018). Balancing flood risk and water supply in California: Policy search integrating short-term forecast ensembles with conjunctive use. *Water Resources Research*, *54*(10), 7557–7576. https://doi.org/10.1029/2018wr023177

Neelin, J. D., Munnich, M., Su, H., Meyerson, J. E., & Holloway, C. E. (2006). Tropical drying trends in global warming models and observations. *Proceedings of the National Academy of Sciences*, *103*(16), 6110–6115. https://doi.org/10.1073/pnas.0601798103

O'Gorman, P. A., & Schneider, T. (2009). The physical basis for increases in precipitation extremes in simulations of 21st-century climate change. *Proceedings of the National Academy of Sciences*, *106*(35), 14773–14777. https://doi.org/10.1073/pnas.0907610106

Ombadi, M. (2026). Data_and_Code for Ombadi et al. Increased Dependency on Extreme Precipitation in a Warmer Climate. *Figshare*. [Dataset]. https://doi.org/10.6084/m9.figshare.31220725.v1

Ombadi, M., Risser, M. D., Rhoades, A. M., & Varadharajan, C. (2023). A warming-induced reduction in snow fraction amplifies rainfall extremes. *Nature*, *619*(7969), 305–310. https://doi.org/10.1038/s41586-023-06092-7

Pall, P., Allen, M. R., & Stone, D. A. (2006). Testing the clausius–clapeyron constraint on changes in extreme precipitation under co2 warming. *Climate Dynamics*, *28*(4), 351–363. https://doi.org/10.1007/s00382-006-0180-2

Pandey, D. N., Gupta, A. K., & Anderson, D. M. (2003). Rainwater harvesting as an adaptation to climate change. *Current Science*, 46–59.

Pendergrass, A. G. (2018). What precipitation is extreme? *Science*, *360*(6393), 1072–1073. https://doi.org/10.1126/science.aat1871

Pendergrass, A. G. (2020). The global-mean precipitation response to co2-induced warming in cmip6 models. *Geophysical Research Letters*, *47*(17), e2020GL089964. https://doi.org/10.1029/2020gl089964

Pendergrass, A. G., & Hartmann, D. L. (2014). The atmospheric energy constraint on global-mean precipitation change. *Journal of Climate*, *27*(2), 757–768. https://doi.org/10.1175/jcli-d-13-00163.1

Pendergrass, A. G., & Knutti, R. (2018). The uneven nature of daily precipitation and its change. *Geophysical Research Letters*, *45*(21), 11–980. https://doi.org/10.1029/2018gl080298

Peng, C., Ma, Z., Lei, X., Zhu, Q., Chen, H., Wang, W., et al. (2011). A drought-induced pervasive increase in tree mortality across canada's boreal forests. *Nature Climate Change*, *1*(9), 467–471. https://doi.org/10.1038/nclimate1293

Pfahl, S., O'Gorman, P. A., & Fischer, E. M. (2017). Understanding the regional pattern of projected future changes in extreme precipitation. *Nature Climate Change*, *7*(6), 423–427. https://doi.org/10.1038/nclimate3287

Rajah, K., O'Leary, T., Turner, A., Petrakis, G., Leonard, M., & Westra, S. (2014). Changes to the temporal distribution of daily precipitation. *Geophysical Research Letters*, *41*(24), 8887–8894. https://doi.org/10.1002/2014gl062156

Reich, P. B., Bermudez, R., Montgomery, R. A., Rich, R. L., Rice, K. E., Hobbie, S. E., & Stefanski, A. (2022). Even modest climate change May lead to major transitions in boreal forests. *Nature*, *608*(7923), 540–545. https://doi.org/10.1038/s41586-022-05076-3

Reich, P. B., Sendall, K. M., Stefanski, A., Rich, R. L., Hobbie, S. E., & Montgomery, R. A. (2018). Effects of climate warming on photosynthesis in boreal tree species depend on soil moisture. *Nature*, *562*(7726), 263–267. https://doi.org/10.1038/s41586-018-0582-4

Rosenzweig, C., Tubiello, F. N., Goldberg, R., Mills, E., & Bloomfield, J. (2002). Increased crop damage in the Us from excess precipitation under climate change. *Global Environmental Change*, *12*(3), 197–202. https://doi.org/10.1016/s0959-3780(02)00008-0

Seager, R., Neelin, D., Simpson, I., Liu, H., Henderson, N., Shaw, T., et al. (2014). Dynamical and thermodynamical causes of large-scale changes in the hydrological cycle over North America in response to global warming*. *Journal of Climate*, *27*(20), 7921–7948. https://doi.org/10.1175/jcli-d-14-00153.1

Seneviratne, S. I., Zhang, X., Adnan, M., Badi, W., Dereczynski, C., Di Luca, A., et al. (2021). Weather and climate extreme events in a changing climate. chapter 11).

Teluguntla, P., Thenkabail, P., Oliphant, A., Gumma, M., Aneece, I., Foley, D., & McCormick, R. (2023). Landsat-derived global rainfed and irrigated-cropland product 30 m v001. *NASA EOSDIS Land Processes Distributed Active Archive Center*. https://doi.org/10.5067/COMMUNITY/LGRIP/LGRIP30.001

Trenberth, K. E. (1999). Climatic change. *Climatic Change*, *42*(1), 327–339. https://doi.org/10.1023/a:1005488920935

Trenberth, K. E., Dai, A., Rasmussen, R. M., & Parsons, D. B. (2003). The changing character of precipitation. *Bulletin of the American Meteorological Society*, *84*(9), 1205–1218. https://doi.org/10.1175/BAMS-84-9-1205

Vogel, E., Donat, M. G., Alexander, L. V., Meinshausen, M., Ray, D. K., Karoly, D., et al. (2019). The effects of climate extremes on global agricultural yields. *Environmental Research Letters*, *14*(5), 054010. https://doi.org/10.1088/1748-9326/ab154b

Wang, J. A., Baccini, A., Farina, M., Randerson, J. T., & Friedl, M. A. (2021). Disturbance suppresses the aboveground carbon sink in north American boreal forests. *Nature Climate Change*, *11*(5), 435–441. https://doi.org/10.1038/s41558-021-01027-4

Wang, Y., Hogg, E. H., Price, D. T., Edwards, J., & Williamson, T. (2014). Past and projected future changes in moisture conditions in the Canadian boreal forest. *The Forestry Chronicle*, *90*(5), 678–691. https://doi.org/10.5558/tfc2014-134

Wasko, C., Nathan, R., Stein, L., & O'Shea, D. (2021). Evidence of shorter more extreme rainfalls and increased flood variability under climate change. *Journal of Hydrology*, *603*, 126994. https://doi.org/10.1016/j.jhydrol.2021.126994

Westra, S., Fowler, H. J., Evans, J. P., Alexander, L. V., Berg, P., Johnson, F., et al. (2014). Future changes to the intensity and frequency of short-duration extreme rainfall: Future intensity of sub-daily rainfall. *Reviews of Geophysics*, *52*(3), 522–555. https://doi.org/10.1002/2014rg000464

Zhang, W., Villarini, G., Vecchi, G. A., & Smith, J. A. (2018). Urbanization exacerbated the rainfall and flooding caused by hurricane harvey in Houston. *Nature*, *563*(7731), 384–388. https://doi.org/10.1038/s41586-018-0676-z

Zhao, T., Zhao, J., Lund, J. R., & Yang, D. (2014). Optimal hedging rules for reservoir flood operation from forecast uncertainties. *Journal of Water Resources Planning and Management*, *140*(12), 04014041. https://doi.org/10.1061/(asce)wr.1943-5452.0000432

Zhu, X., & Troy, T. J. (2018). Agriculturally relevant climate extremes and their trends in the world's major growing regions. *Earth's Future*, *6*(4), 656–672. https://doi.org/10.1002/2017ef000687